

The Characterization of C-Rate Dependent Hard Carbon Anode  
Fracture Induced by Lithium Intercalation

by

Thomas A. Villalón Jr.

Submitted to the  
Department of Materials Science and Engineering  
in Partial Fulfillment of the Requirements for the Degree of

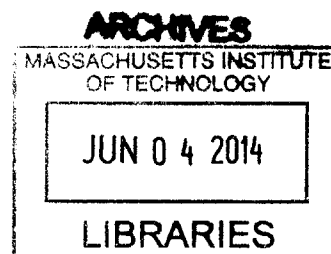
Bachelor of Science

at the

Massachusetts Institute of Technology

June 2014

© 2014 Thomas A. Villalón Jr.  
All rights reserved



The author hereby grants to MIT permission to reproduce and to  
distribute publicly paper and electronic copies of this thesis document in whole or in part  
in any medium now known or hereafter certified.

**Signature redacted**

Signature of Author.....

Department of Materials Science and Engineering  
May 9, 2014

**Signature redacted**

Certified by.....

Yet-Ming Chiang  
Kyocera Professor of Ceramics, Department of Materials Science and Engineering  
Thesis Supervisor

**Signature redacted**

Accepted by.....

Jeffrey C. Grossman  
Carl Richard Soderberg Associate Professor of Power Engineering  
Chairman, Undergraduate Thesis Committee

# The Characterization of C-Rate Dependent Hard Carbon Anode Fracture Induced by Lithium Intercalation

by

Thomas A Villalón Jr.

Submitted to the  
Department of Materials Science and Engineering  
in Partial Fulfillment of the Requirements for the Degree of  
Bachelor of Science at the Massachusetts Institute of Technology

May 9<sup>th</sup>, 2014

© 2014 Thomas A. Villalón Jr.  
All rights reserved

## ABSTRACT

This study sought to evaluate hard carbon's fracture characteristics under different cycling rates due to its lithium solid solubility and isotropic nature. In addition to the evaluation, an electrochemical shock map was modified from a previous study to try and predict what conditions of particle size and C-rate are necessary to cause brittle fracture events in hard carbon. Subsequently, hard carbon anodes were created using a formulation of hard carbon, carbon black, and Kureha binder and subjected to two or three cycles of C-rates varying from  $\frac{C}{10}$  to 5 C.

Data evaluation suggests that for every C increase approximately nine more percent of the particles in the system will develop cracks. Further analysis of the data shows that low C-rate anodes may have been affected by inhomogeneous mixtures, skewing the linear relationship to a higher than accurate value in the linear plot. Additionally, a C-rate limit that prevents any brittle fracture from occurring can be found at  $\frac{C}{10}$  or lower. When comparing the anodes to the model, the model shows accuracy in predicting failure conditions for the higher C-rate anodes. When applied to lower C-rates (below  $\frac{C}{2}$ ), the accuracy of the model begins to fall. Possible solutions to this problem include finding more accurate material properties for hard carbon or redefining the model to account for some unique value (i.e. – the hard carbon's geometry) associated with the hard carbon. Additionally, more anodes should be tested to create a larger sampling that can average cells that have inhomogeneous mixtures.

Thesis Supervisor: Yet-Ming Chiang

Title: Kyocera Professor of Ceramics, Department of Materials Science and Engineering

# Acknowledgements

Prof. Chiang,

Thank you for inspiring me in your ceramics class to commit myself to research and giving me the opportunity to investigate this set of materials. It was the opportunity of a lifetime. Through this work, I got to understand the nature of research. To say the least, it was a whirlwind experience and it will remain with me for years to come.

Dr. Woodford IV,

Thank you for helping me understand the research material and gain a new insight into the field of materials science and battery. Without you, this work would not be possible. I can't thank you enough for all your help and wish you the best in your future endeavors.

To my family and friends,

Thank you for your support in my time at MIT. Without y'all, I wouldn't be where I am today. May God bless y'all as each one of you continues on your path through life.

Orbis Non Sufficit  
- Thomas Villalón Jr.

# Table of Contents

<b>1. List of Figures and Tables.....</b>	<b>5</b>
<b>2. Section I – Introduction.....</b>	<b>9</b>
<b>3. Section II – The Mechanics of Battery Electrodes.....</b>	<b>14</b>
2.1. Section II.A – Intercalation Effects of Lithium Ions.....	14
2.2. Section II.B – C-rate Effects.....	16
2.3. Section II.C – Fracture Events and Theoretical Model.....	17
<b>4. Section III – Properties of Hard Carbon.....</b>	<b>20</b>
3.1. Section III.A – Intercalation into Hard Carbon.....	20
3.2. Section III.B – Hard Carbon Fracture.....	21
<b>5. Section IV –Experimental Setup, Results, and Analysis.....</b>	<b>23</b>
4.1. Section IV.A – Experimental Setup.....	23
4.2. Section IV.B – Cycling Data and SEM Images.....	24
4.4. Section IV.C – Diffusion Based Current Spikes.....	33
4.5. Section IV.D – Fracture Count Data Analysis.....	34
4.6. Section IV.E – Results Comparison to Theoretical Model.....	39
<b>6. Section V – Conclusion.....</b>	<b>42</b>
<b>7. Section VI – Citations.....</b>	<b>43</b>

# List of Figures and Tables

## Figures:

1. Figure 1 – A Simplified Electrochemical Cell – Image shows the basic flow of ions and electrons while demonstrating the components and configuration of an electrochemical system.....10
2. Figure 2 – Lithium Manganese Oxide Electrochemical Shock Map – Figure shows conditions under which fracture events are likely to occur.....12
3. Figures 3a and 3b – Lithium Cobalt Oxide (Left) and Lithiated Graphite (Right) – Images shows the ability of lithium to intercalate into structures in a layered manner; images from <http://upload.wikimedia.org/wikipedia/commons/5/57/Lithium-cobalt-oxide-3D-balls.png> and <http://upload.wikimedia.org/wikipedia/commons/4/40/Potassium-graphite-xtal-3D-SF-C.png>.....14
4. Figure 4 – Lithium Induced Electrochemical Shock via Flow Process – Image shows plastic deformation that occurs after a cycling process takes place..15
5. Figure 5a and 5b - System With Adequate Diffusion (Left), System With Diffusion Gradient (Right) – Left image shows a system where diffusion can handle the amount of intercalating lithium; Right image shows a system where a diffusion gradient has formed along with a local displacement.....16
6. Figure 6 – Hard Carbon Electrochemical Shock Map – Image shows a model that attempts to predict the conditions where hard carbon particles begin to fracture, lines A and B represent the low and high bounds for fracture conditions, respectively; image from Woodford et al, 2010.....18
7. Figure 7 – Non-intercalated Carbotron Particles – A control image of the Carbotron hard carbon.....24

8. Figure 8 – A Non-intercalated Composite Anode – A control image of an anode that has not undergone cycling.....26

9. Figure 9 – Cycling Data for a  $\frac{C}{10}$  Anode – Images shows three  $\frac{C}{10}$  cycles of data in an exemplar anode.....27

10. Figure 10 – SEM Image for a  $\frac{C}{10}$  Anode – Images shows a cycled  $\frac{C}{10}$  anode.....27

11. Figure 11 – Cycling Data for a  $\frac{C}{5}$  Anode – Images shows three  $\frac{C}{5}$  cycles of data in an exemplar anode.....28

12. Figure 12 – SEM Image for a  $\frac{C}{5}$  Anode – Images shows a cycled  $\frac{C}{5}$  anode.....29

13. Figure 13 – Cycling Data for a  $\frac{C}{2}$  Anode – Images shows three  $\frac{C}{5}$  cycles of data in an exemplar anode.....30

14. Figure 14 – SEM Image for a  $\frac{C}{2}$  Anode – Images shows a cycled  $\frac{C}{2}$  anode.....31

15. Figure 15 – Regions of High Intensity Intercalation – Image shows an outlined area where a high contrast is visible; most likely SEI has formed in the area due to high C-rates; possible cause is uneven surface contact with lithium foil, creating area of higher-than-nominal C-rate.....31

16. Figure 16 – Cycling Data for a  $5C$  Anode – Images shows three  $5C$  cycles of data in an exemplar anode.....32

17. Figure 17 – SEM Image for a  $5C$  Anode – Images shows a cycled  $5C$  anode, note the large amount of cracking present.....33

18. Figure 18 – Exemplar Image with Highlighted Cracks – Image is example with highlighted cracks to demonstrate how particles were analyzed.....35

- 19. Figure 19 – Plot of Percentage of Cracked Particles as a Function of C-rate – Plot shows the percentage of cracks as C-rate increases.....37
- 20. Figure 20 – Plot Analysis of Figure 19 – Image shows the numerical values associated with the plot in Figure 19; numbers show a correlation between C-rate and the number of cracks.....37
- 21. Figure 21 – Hard Carbon Electrochemical Shock Map Check – Image compares theoretical model to data points observing in SEM imaging.....39

**Tables:**

- 1. Table 1 – Material Properties Input into Electrochemical Shock Model – Table displays values used in determining the new hard carbon electrochemical shock map.....18
- 2. Table 2 – Summary of Data Collected – A summary of relevant data derived from the SEM image analysis of the anodes.....36

Characterization of Hard Carbon Anode Fracture Mechanics  
Induced by Variable C-Rate Lithium Intercalation

Thomas A. Villalón Jr.



# Section I

## Introduction

The goal of a materials scientist is to characterize new materials based on their structure, properties, performance, and how they were processed. This knowledge is then used to make a system where the material can be used to its full potential. In the modern world, this process is vital to the field of energy storage. As the global demand for electricity becomes higher and higher, the ability to store excess electricity in small portable electronic devices or grid-scale units is continuously increasing. As a result, innovative electrochemical storage technologies need to be developed to cope with the potential future demand. So, an increasingly important question for materials scientists is, "What materials can be used to create new energy storage systems that supersede our current technologies?"

Batteries are a particular form of energy storage technology that that rely on new materials to create more powerful or energy-dense units. They are a system where ions, typically lithium ions in high-end batteries, are initially displaced from a cathode into an anode, storing energy in the form of ions that seek to return to a lower electrochemical potential (Warne, 2005). This creates a potential in the system between the cathode and the anode. To prevent the system from immediately reverting to its uncharged state, a polymer separator is used to keep the ions from readily moving between the electrodes. When the electrodes are connected by an external circuit, the electrons can move from the anode to the cathode. This flow of electrons powers an external circuit which can produce work elsewhere as a consequence of the energy stored earlier. Meanwhile, the ions associated with the moving

electrons migrate through the separator via an electrolyte, meeting with the electrons at the cathode. To reverse this process and recharge the battery, a voltage is placed on the external circuit, forcing the electrons and ions to return to the anode (Warne, 2005). A diagram depicting this can be seen in **Figure 1**.

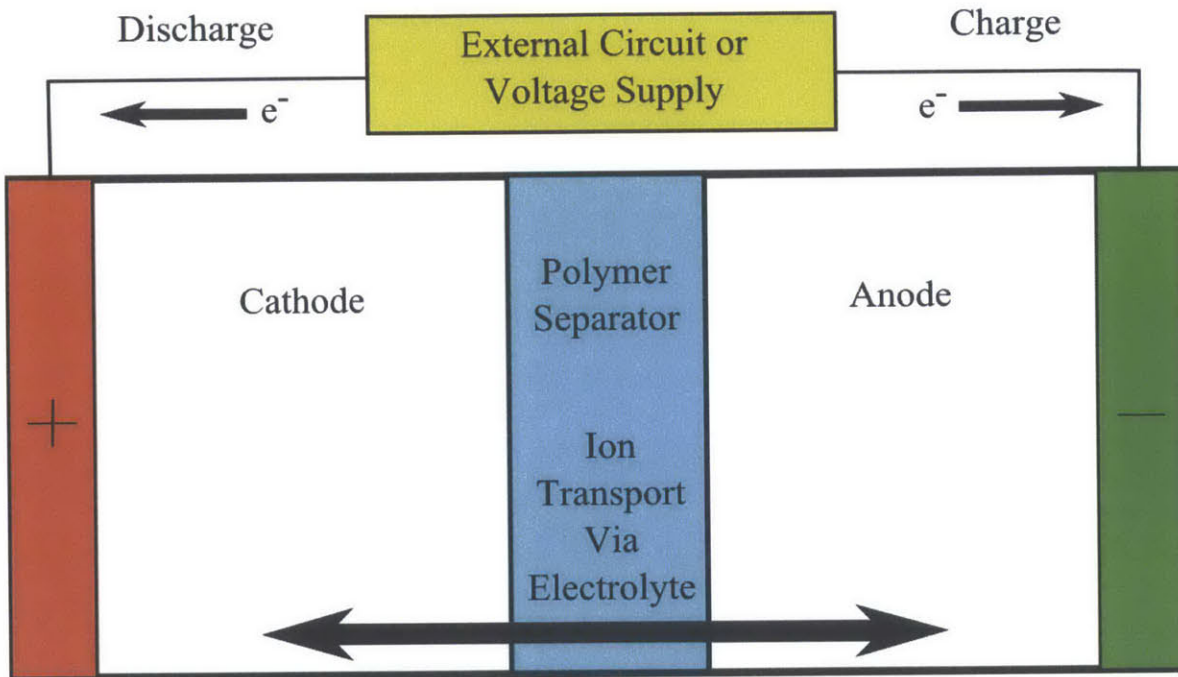


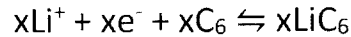
**Figure 1 – A Simplified Electrochemical Cell**

In the case of lithium batteries, an exemplar electrochemical cell can be composed of a lithium cobalt oxide cathode, a lithium hexafluorophosphate electrolyte, and a graphite anode (Marom et al, 2011). Assuming that overpotential reactions do not occur, this system is then defined by the following reactions at the positive and negative electrodes, the cathode and anode respectively. At the cathode, the following half-cell reaction applies:



**Equation 1 – Nominal Half Cell Reaction at a Lithium Cobalt Oxide Cathode**

The opposing reaction at the anode is the following:



### Equation 2 – Nominal Half Cell Reaction at a Graphite Anode

This systems operates under the assumption that the lithium is reversibly exchanged from one electrode to another. However, it should be noted that these ideal systems can break down over time in real world circumstances due to effects such as solid electrolyte interphase (SEI) formation and electrode brittle fracture (Marom et al, 2011). SEI is the result of the system's electrolyte reacting with an electrode's material, creating an ion intercalation barrier (Tasaki et al, 2009). The details of brittle fracture will be discussed more in depth in **Section II** of this document.

As a consequence of a battery's structure and function, there are design constraints and physical limitations to what a battery can achieve. In the case of lithium batteries, this problem can be seen in the anode materials. Currently, graphite is considered to be the anode material of choice because it a material that meets a compromise of cost, usability, and safety (Marom et al, 2011). Briefly, it is cheap compared to other materials, it has a relatively high reversible capacity, and does not pose an immediate threat to a user if exposed to air. However, it has two potential issues that hinder it performance. One is that it has a limited charge capacity, approximately  $372 \frac{\text{mAh}}{\text{g}}$ , based on the maximum possible solubility of lithium in graphite (Kureha, 2013; Agruba et al, 2013). This limit is the compound  $\text{LiC}_6$ . The other issue is that over time, it begins to break down due to large amount of cycling or high C-rate lithium ion insertion

(Agruba et al, 2013). This phenomenon can be attributed to the fracture, or “electrochemical shock”, of the graphite particles as more cycling occurs due to diffusion based stresses (Grantab et al, 2011, Woodford et al, 2010). This then leads to the formation of a solid electrolyte interphase (SEI) on the newly exposed faces which prevents the lithium from intercalating onto the new surfaces. The fracture of graphite particles causes a loss of intercalation sites for the lithium ions to use, lowering the capacity of the anode. These fracture events also occur in other electrodes of different materials as well. One studied example of this is event is the brittle fracture of lithium cobalt oxide. In a study conducted by Dr. William Woodford IV, a model was produced that could predict the conditions required for brittle fracture events to occur (Woodford et al, 2010). This model can be seen in **Figure 2**.

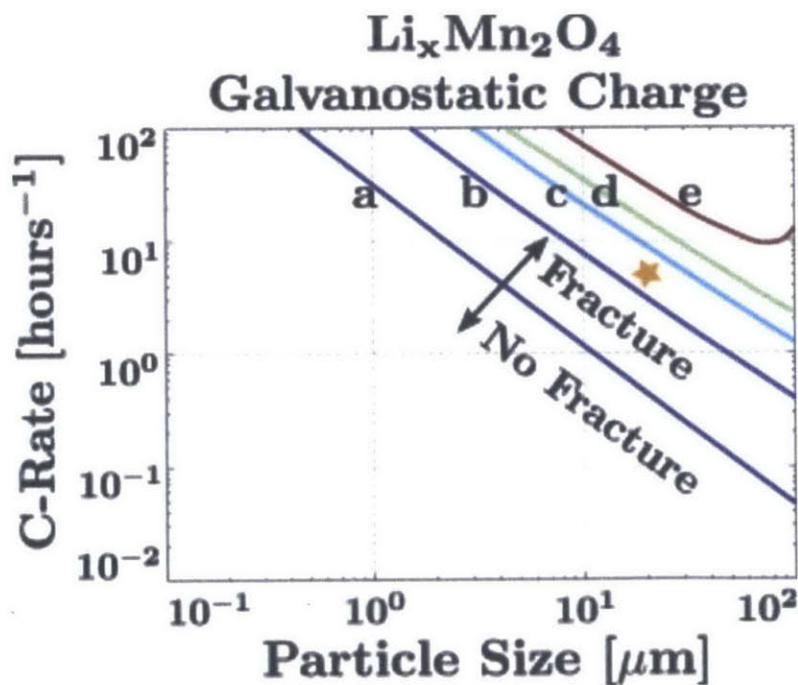


Figure 2 – Lithium Manganese Oxide Electrochemical Shock Map

Since this phenomena is present in many materials, it prompts the question if better, more mechanically sound materials exist. In the case of anode materials, it prompts the question if a material exists that has a higher capacity and more mechanical toughness than graphite.

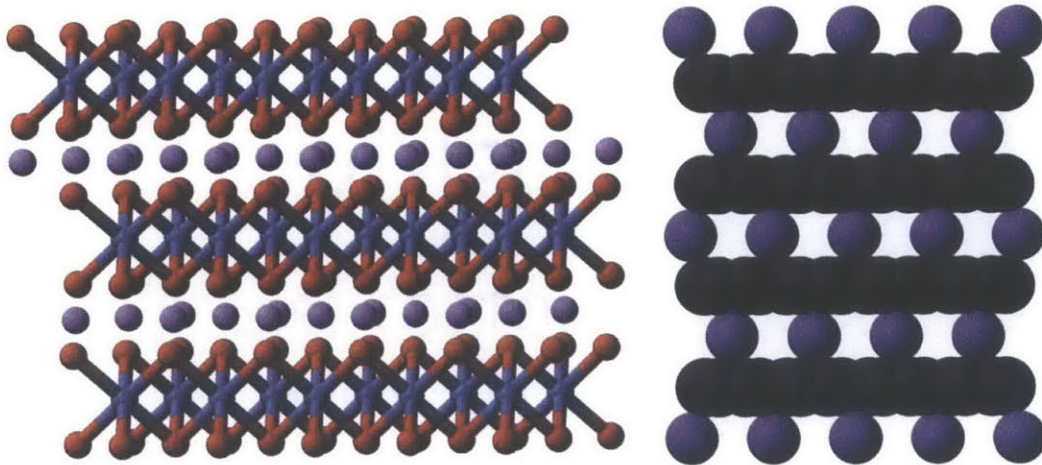
As a result of this question, researchers have begun looking into new anode materials. For this particular thesis, a novel hard carbon structure will be characterized at different rates of charge and discharge. The basis for this is the assumption that the hard carbon can create a solid solution with lithium that is not limited to a  $\text{LiC}_6$  composition, allowing rate dependent mechanical failure to be analyzed via the aforementioned electrochemical shock map. Additionally, the amorphous hard carbon allows an isotropic system to be studied in rate varying conditions. In theory, this material would allow for a higher capacity and better cycling characteristics to exist within the anode, leading to higher performance in a battery. To fully understand this, the following section will be devoted to exploring the technical details of how a battery kinetics and mechanics work. After that, the characteristics of the novel hard carbon material will be explored. Subsequently, the procedures for anode creation, experiment results, and data analysis will be stated. Finally, all the data will be put into the larger context of electrochemical energy storage.

## Section II

### The Mechanics of Battery Electrodes

#### Section II.A – Intercalation Effects of Lithium Ions

One of the key principles that batteries operate on is intercalation. Intercalation is the process that allows ions or molecules to move in or out between other structures. In the case of batteries, this process is evident in both the anode and cathode. Typically both structures are layered crystalline structures (Bottani et al, 2008). An example is presented in **Figures 3a and 3b** with the lithium cobalt oxide structure on the left and the graphite structure on the right.



**Figures 3a and 3b – Lithium Cobalt Oxide (Left) and Lithiated Graphite (Right)**

When in operation, a battery functions on the movement of ions and electrons. This phenomena has two different effects, one on the cathode and one on the anode. In the case of an initially lithiated anode, the potential created by the electrochemical cell begins to draw lithium ions from the anode surface. Once the surface layers have been depleted, the system must begin drawing on ions that are further within the structure, creating diffusion gradients



within the graphite (Brassart et al, 2012). As the diffusive process draws from more ions from within the crystalline structure, one of two inelastic processes may occur: flow or reaction (Brassart et al, 2012). In the flow process, the stoichiometry of the system remains the same, but the volume of the system changes by the loss of local atoms causing a stress to develop. In the reaction process, the stoichiometry of the system begins to change causing both a volumetric and potential change in the system, leading to a stress in the newly changed area (Brassart et al, 2012; Zhang et al, 2008). In either event, plastic deformation occurs on the electrode leading to conditions that can lead to fractures developing on the electrode with intercalation occurs again (Hu et al, 2010). An example of this can be seen in **Figure 4**.

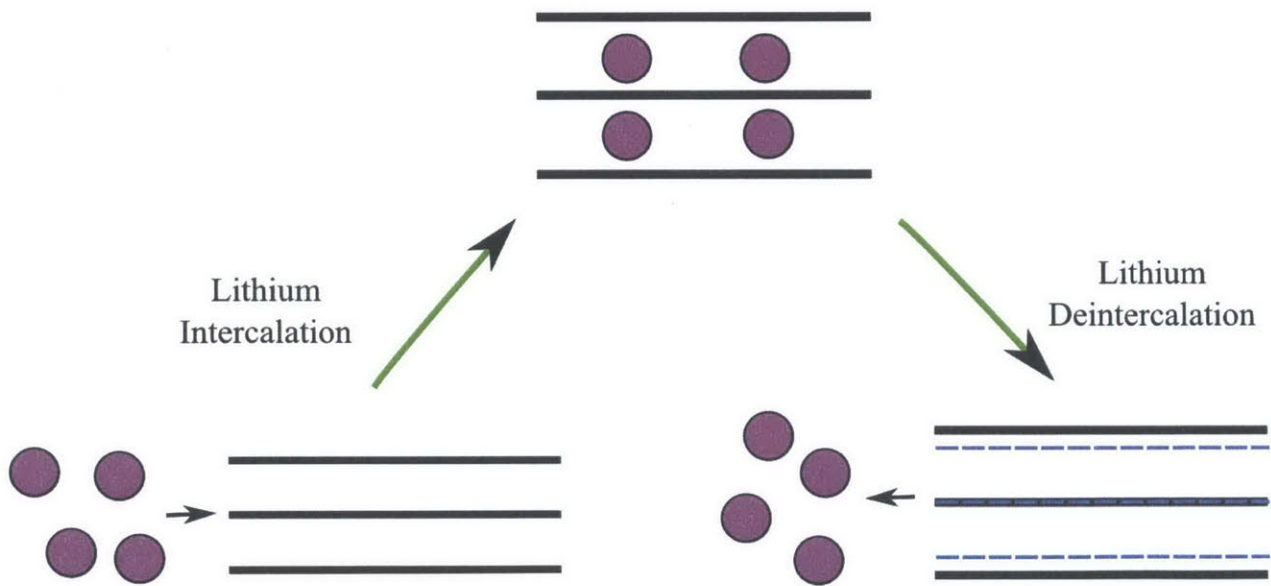


**Figure 4 – Lithium Induced Electrochemical Shock via Flow Process**

As the system is intercalated and deintercalated, the plastic deformation continues to compound, seen as the difference in spacing between the black and dashed blue lines in **Figure 4**. This eventually leads to a stressed state that the material cannot handle, creating a fracture event (Marom et al, 2011).

## Section II.B – C-rate Effects

Besides cycling causing plastic deformation on the electrode particles, the C-rate of a system can also induce stresses via diffusion gradients (Zhao et al, 2010). The C-rate of a system is the current at which an electrode charge or discharges in  $\frac{1}{C}$  hours where C is a specified number of hours per charge or discharge (Klink, 2013). In a diffusion based intercalation environment, a high C-rate creates a gradient of lithium ions on a particle surface. By applying a high enough C-rate, graphite and other carbonaceous materials cannot homogenize the intercalation of lithium quickly (Zhao et al, 2010). This leads to a gradient of lithium ions forming on the material's surface and can potentially cause a fracture via a flow or reaction process (Markovsky et al, 1998; Brassart et al, 2012). An image showing displacement,  $\delta$ , caused by a diffusion gradient can be seen in **Figure 5b** with a system that can adequately diffuse lithium in

**Figure 5a.**

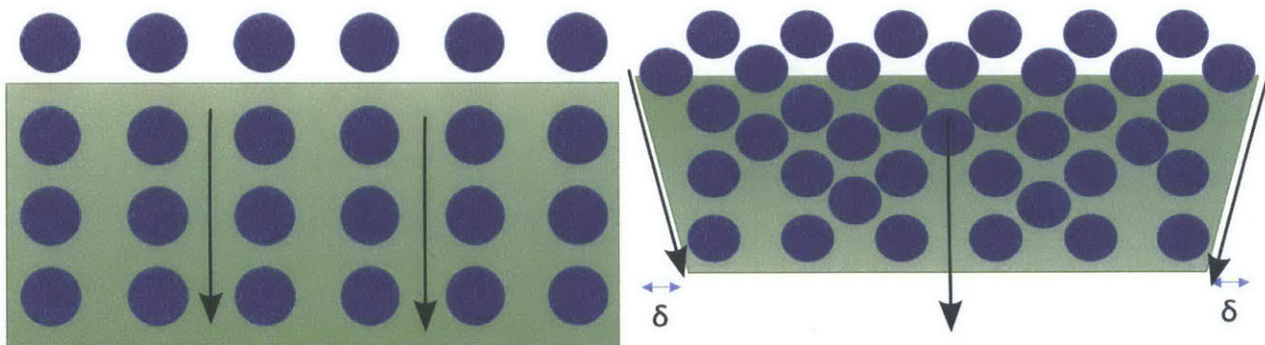


**Figure 5a and 5b – System With Adequate Diffusion (Left), System With Diffusion Gradient (Right)**



## Section II.C – Fracture Events and Theoretical Model

In the event of high stress buildup, a threshold stress will be reached which can cause the electrode material to fracture either partially or completely (Rapoport et al, 1998). Due to the amorphous nature of the hard carbon studied, the ability to calculate a threshold crack stress with equations typically used for metals is impossible due to the lack of grain boundaries. However, an estimation can be made using models already developed for electrode materials. Using the framework of the model developed by Woodford, an electrochemical shock map was developed in an attempt to predict the conditions where the hard carbon may fracture. Prior to using this model, a series of assumptions must be made. The first assumption is that the irregularly shaped hard carbon will behave similarly to a crystalline sphere. This can be justified by the aspect ratio of the hard carbon. Since the carbon particles can be associated with a cube shape, more particularly the smaller pieces, they can be assumed to have an aspect ratio of approximately 1:1. This conforms to the sphere shape assumption made in the model that aspect ratios be approximately 1:1. Additionally, the hard carbon will be undergoing expansion and contraction stresses due to intercalation effects and diffusion gradients. This means that mode 1 failure is more likely to occur since shear stresses will be negligible compared to stresses parallel to the plane being examined (Brassart et al, 2012; Sgvalo et al, 1996). For glassy, carbonaceous materials, a mode 1 stress intensity factor ranges from 0.76 to 1.08  $MPa * \sqrt{m}$  (Nadeau, 1974). Using the variables of C-rate, particle size, and stress intensity factor, the map was created and can be seen in **Figure 6** while the material properties used to generate the map can be seen in **Table 1**. It should be noted that all of the material values are

estimates dealing with other forms of hard carbon. Therefore, these properties may not truly reflect the hard carbon used in the experiment, but instead provide a rough estimate.

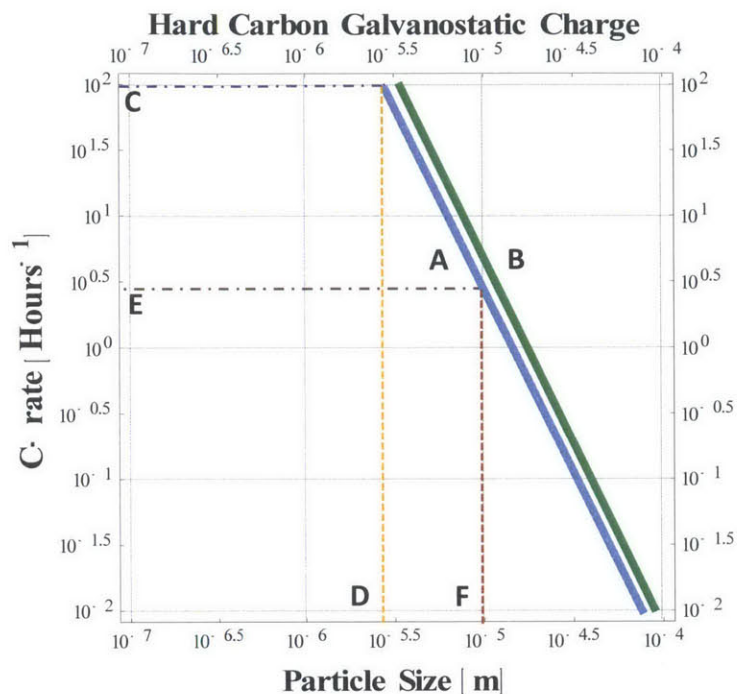


Figure 6 – Hard Carbon Electrochemical Shock Map

Material Property	Value	Source
Young's Modulus	$59 \times 10^3 \text{ MPa}$	Pharr et al, 1995
Poisson's Ratio	0.3	Woodford et al, 2010
Diffusivity of Lithium	$1.4 \times 10^{-10} \text{ MPa}$	Guo et al, 2007
Maximum Lithium Concentration	$2.44 \times 10^4 \frac{\text{mol}}{\text{m}^3}$	Kureha Corporation, 2013
Density	$1.52 \frac{\text{g}}{\text{cm}^3}$	Kureha Corporation, 2013
Theoretical Capacity	$430 \frac{\text{mAh}}{\text{g}}$	Kureha Corporation, 2013
Stress Intensity Factor	$0.76 \text{ to } 1.08 \text{ MPa} * \sqrt{\text{m}}$	Nadeau, 1974

Table 1 – Material Properties Input into Electrochemical Shock Model

The blue line labeled, **A**, indicates the lower bound of the fracture range based on the data provided by Nadeau. The green line labeled, **B**, shows the higher bound of the conditions required for fracture. The area in between the two curves gives an indication of where fracture is to occur. Analyzing the lower boundary, it can be estimated that a C-rate of above 100 is required to fracture particles that are 2.5 micrometers in diameter or lower as seen by the intersection of lines **C** and **D**. However, once particles reach a size of ten micrometers, they are susceptible to fracture at a C-rate of 0.355. This can be seen in the intersection of lines **E** and **F**. Using the conservative values from the model then, any particles smaller than 10 micrometers should not fracture at C-rates below  $0.355C$ .

## Section III

### Mechanical Principles of Hard Carbon

#### Section III.A – Intercalation into Hard Carbon

As a consequence of these effects in crystalline structures, new interest in amorphous materials has arisen. The idea is that the lack of crystalline structure and larger interlayer spacing will prevent fracture from occurring along weak points in the crystal structure, specifically crystal planes. To allow for intercalation to occur in amorphous materials, a new model is required to understand the diffusion mechanics. For hard carbon, J.R. Dahn and associates have proposed a model that describes the amorphous carbon like a house of cards (Stevens et al, 2000). The structure is a series of small aromatic fragments that are stacked on top of each other in random orientations relative to other local fragments. It is hoped that the large surface area of this structure can lead to the creation of anodes that surpasses the capacity of graphite due to the presence of pores. The presence of pores on the hard carbon acts similar to adsorption sites, collecting larger quantities of lithium compared to more uniform structures (Stevens et al, 2001). As a consequence of these phenomena, hard carbon does not experience the same hard stop while intercalating lithium, leading to an increased theoretical charge capacity (Azuma et al, 1999). However, unlike graphite, when it is discharging lithium, hard carbon has the system voltage decrease when nearing the end of a discharge event.

Similar to graphite, the lithium ions intercalate into the hard carbon structure via diffusion and find sites to inhabit. However, the average spacing between layers is approximately 0.38 *nm*

(Nishi, 2001). This allows the lithium to theoretical move in and out freely of the hard carbon. Also, due to the random orientation of the aromatic segments, the lithium ions do not inhabit the carbon in a uniform fashion (Stevens et al, 2001). This creates a scenario where the expansion and thus stressing of hard carbon (i.e. – a flow process) should not be problematic unless a large diffusion gradient is created. However, local potentials can develop within the hard carbon’s porous structure, altering how the lithium ions diffuse into the carbon (Azuma et al, 1999). This could possibly create diffusion gradients on a surface of the particulate, negatively affecting the performance of the anode.

## Section III.B – Hard Carbon Fracture

Similar to graphite, hard carbon can encounter diffusion gradients if high C-rates are encountered. These diffusion gradients can then act as the catalysts for fracture events. By accumulating large amounts of lithium ions locally one of two events can occur. The first event is a change of composition which can then lead to a local change of structure. This induces a stress according to the reaction process mentioned beforehand due to the new compound’s lattice structure (Brassart et al, 2012). In the case of hard carbon, this new compound could be  $\text{LiC}_2$  or some other high lithium soluble carbon-based compound, which may have defined lattice structures that warp nearby surroundings (Azuma et al, 1999; Nalimova et al, 1995). The second event is where a diffusion gradient can also cause a flow reaction to occur at a high enough C-rate. Here, fracture events occur because the large amount of local ions expands the environment as seen in **Figure 5b**. Additionally, due to hard carbon’s amorphous nature, only a small amount of plastic deformation occurs prior to reaching the ultimate stress and fracturing

(Nishi, 2001). This means that any stress buildup can cause a sudden fracture event to occur. This creates a scenario where SEI can form along the faces of the newly exposed carbon, reducing the overall number of sites that can house a lithium ion (Agruba et al, 2013). This reduces the overall capacity of the material. Therefore, hard carbons that are capable of undergoing high C-rate charges and discharges are desirable.

## Section IV

### Experimental Setup, Results, and Analysis

#### Section IV.A – Experimental Setup

Composite anodes were created by mixing together Kureha Carbotron S(F), Super P carbon black, and Kureha's proprietary polymer binder by weight ratios of 90%, 5%, and 5%, respectively. To dilute the polymer binder into a usable slurry, 0.75 mL stock n-methyl-2-pyrrolidone (NMP) was added per batch of 222.1 mg of ingredients mixed. The components were mixed together in a glovebox, put in a small plastic vial, and then agitated by a vortex generator for 5 minutes. The slurry was then cast onto a sheet of aluminum foil and then placed in a ShellLab 1410M vacuum oven. The samples were heated under vacuum at 120° C for at least six hours. The dried powder was scrapped off the foil and ground into a fine powder with a mortar and pestle. The powder was pressed into ¼ inch pellets with a die set and a Carver Hydraulic Unit Model #3912, holding a ton of pressure for two presses that lasted a minute each. The sample's thickness was then measured with a Mitutoyo Absolute Digimatic Indicator ID-C and the samples were put back in the vacuum oven and heated again at 120° C under vacuum for a minimum of two hours. The samples were later weighed and immediately put in an argon environment glovebox. Here, a lithium foil of 0.75 millimeter thickness was punched into 12 millimeter diameter circular pieces. Afterwards, Swagelok cells were created with the pressed anodes, lithium metal pieces, and a 1 molar lithium hexafluorophosphate electrolyte, composed of a 1:2 ratio ethylene carbonate and diethyl carbonate solvent. The cells were then tested with a Solartron Analytical 1470E CellTest System for two or three cycles, recharging the

cell to 2.0 volts after each cycle. Anodes were extracted after testing and imaged using a Philips XL30 Environmental Scanning Electron Microscope (ESEM)-FEG.

## Section IV.B – Cycling Data and SEM Images

Briefly, it is important to note that only select images will be presented in this thesis. If the reader wishes to see the remaining images, please contact Professor Yet-Ming Chiang for the full compilation of images and charge capacity curves.

In order to note the effects of stress inducing intercalation, the anode material must first be characterized in a non-intercalated state. An image of the Kureha Carbotron material is seen in

**Figure 7.**

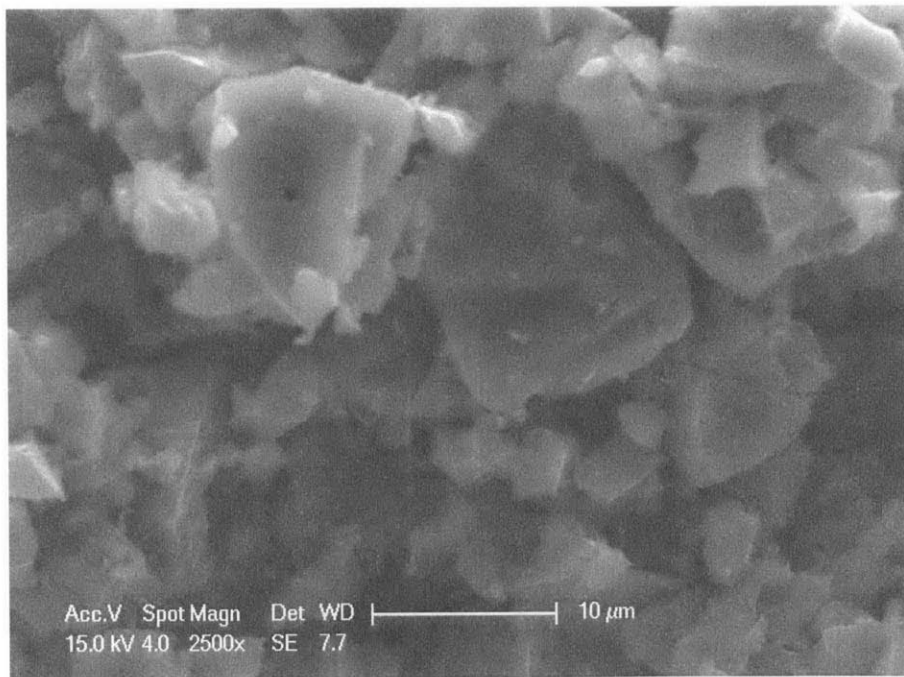


**Figure 7 – Non-intercalated Carbotron Particles**



Due to the particles' amorphous nature and their processing techniques, there are unique characteristics in this system. The first is the variable particle size. In examining several photos, the Carbotron particles size tends to be within the range of two to fifteen micrometers. Documentation indicates an average particle size of 9 micrometers (Kureha, 2013). However, upon further observation, it is also appears that there is no average particle size. The distribution of particle size arranges itself so that either the particles are on the lower end, two to four micrometers, or higher end, thirteen to fifteen micrometers, of the spectrum. Another unique characteristic is the shape and topography of the particles. The particle shape tends to be highly irregular with jagged edges and no discernible crystalline features that could indicate potential fracture lines. The surfaces of the particles also show non-planar surfaces with sporadically located pits or occlusions. The origin of these features is unknown but can be attributed to the pyrolysis process involved in making the amorphous structure. This can be deduced from the practice of making other glassy carbons (Nadeau, 1974). It is also unknown if these pits can occur within the carbon structure.

To understand a non-intercalated composite anode and the system's remaining components, **Figure 8** is presented below.

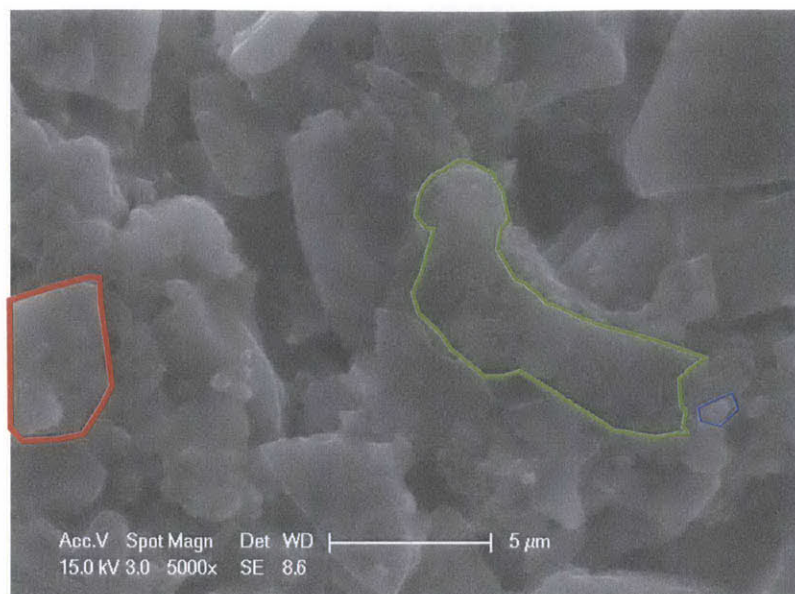
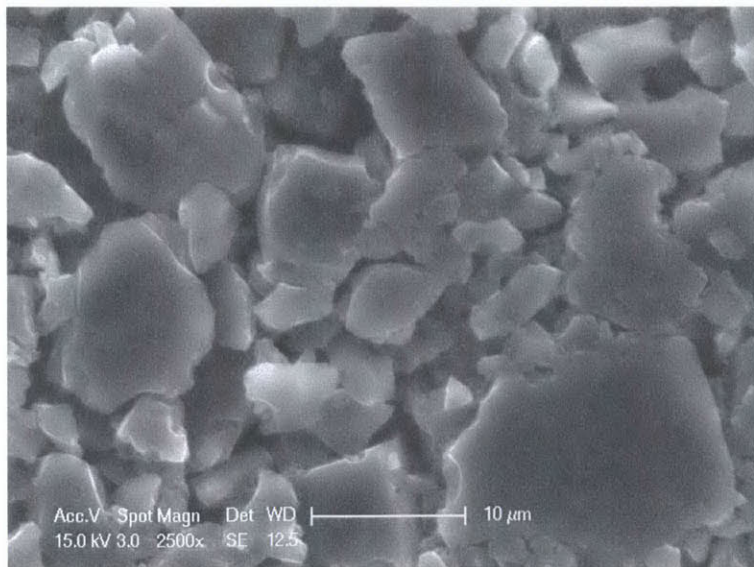
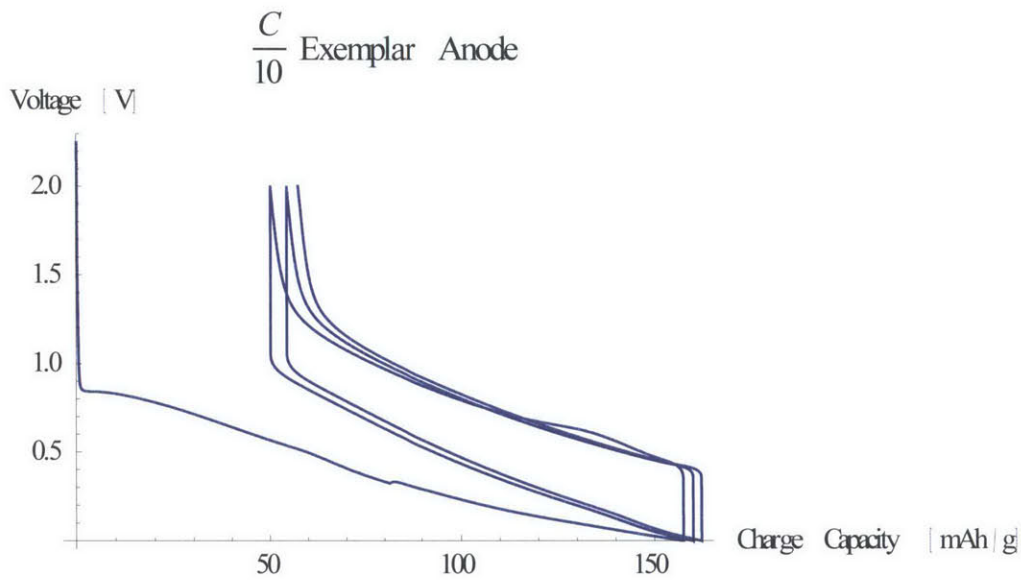


**Figure 8 – A Non-intercalated Composite Anode**

The composite anode shows the three constituent components: the hard carbon (outlined in red), the carbon black (outlined in blue), and the polymer matrix (which appears as the gum-like substance outlined in green). Unlike the previously described hard carbon, the carbon black tends to have spherical or ellipsoidal shaped particles. Besides the difference in shape, the hard carbon particles are larger than the carbon black counterparts. The polymer matrix is the surface connecting the particles together. **Figure 8** shows a mixture of hard carbon, carbon black, and matrix along a three dimensional plane. This indicates a homogenous mixture that should lead to optimal anode performance. Additional images on the surface of the composite anode show a densely packed structure that appear to be planar. This means that full contact between the anode and the lithium metal should be present. This prevents an ion diffusion bottleneck from occurring, allowing for a maximum current to pass in the system.

Due to the model's prediction, a series of sample tests were run, starting with a C-rate of  $\frac{C}{10}$ .

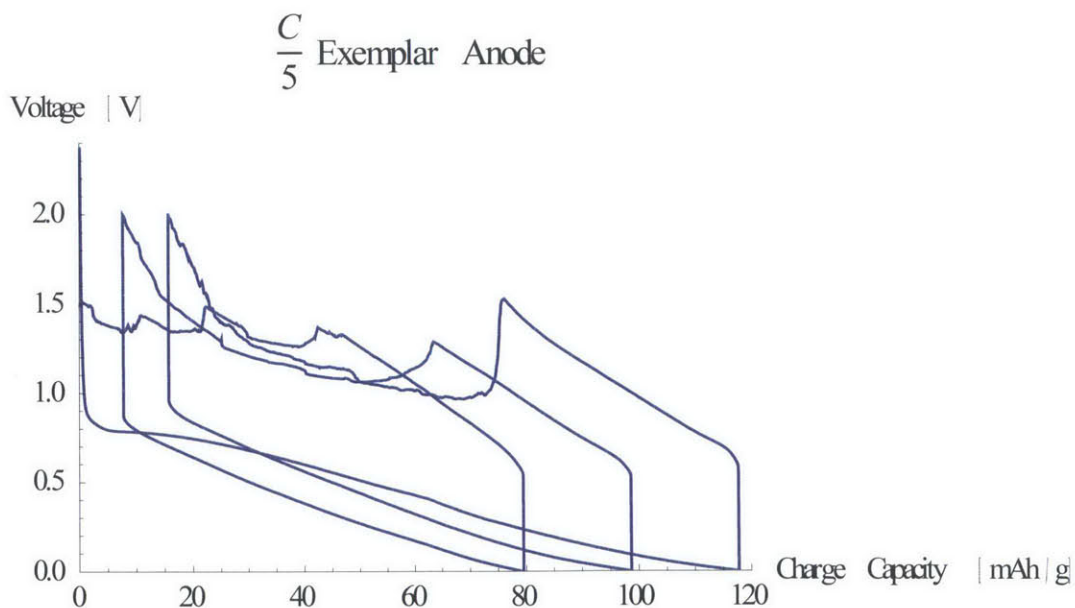
These tests were run with the assumption that the C-rate was so low that the anode should not experience electrochemical shock. Below is an example of cycling data, **Figure 9**, for a  $\frac{C}{10}$  C-rate system along with an image of that sample's anode, **Figure 10**. Each line in **Figure 9** represents a separate cycling event.



**Figures 9 and 10 – Cycling Data and SEM Image for a  $\frac{C}{10}$  Anode**

In this system, the data indicates that the reversible charge capacity over two cycles is approximately  $110 \frac{\text{mAh}}{\text{g}}$ . The remaining charge is irreversibly consumed by the anode, leading to a loss of approximately  $50 \frac{\text{mAh}}{\text{g}}$ . Looking at the SEM Images, no signs of fracture are present. In order to verify this broadly,  $7 \frac{C}{10}$  electrodes were examined in at least separate areas at a constant magnification of 2500X. This created a sample set of 20 images. In the twenty images, only one crack was apparent. The nature of this crack appears to be an isolated event, though. A possible origin for this will be discussed later in **Section IV.C**. All other images give no indication of fractures occurring at this C-rate. This presumably indicates that at or below this C-rate, no fracture will occur in this particular formulation of hard carbon composite anodes.

In the next set of anodes, a C-rate of  $\frac{C}{5}$  is present. The anodes have the following data in **Figure 11** and corresponding images in **Figure 12**.



**Figures 11 - Cycling Data for a  $\frac{C}{5}$  Anode**

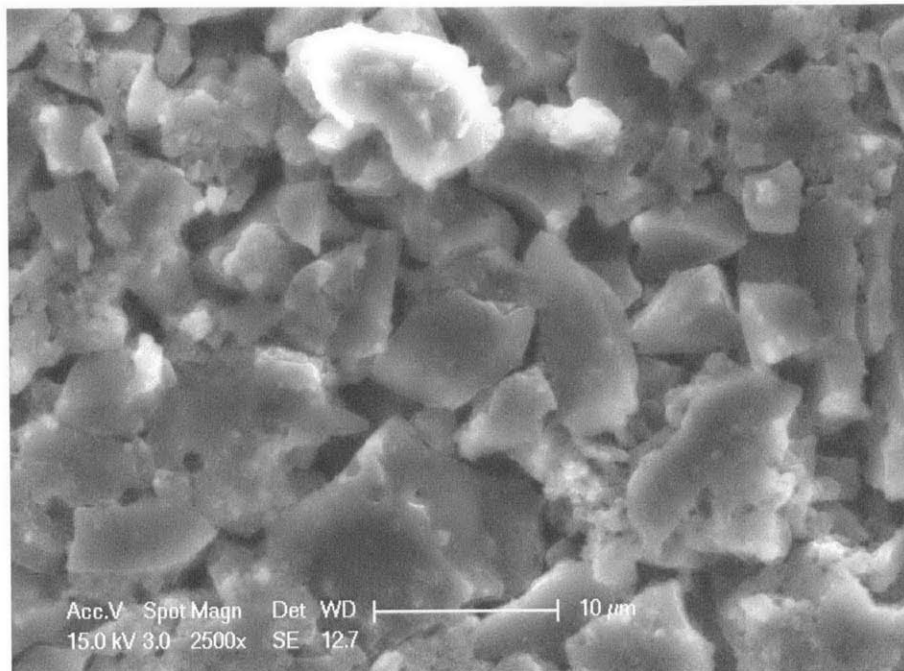


**Figure 12 – SEM Image for a  $\frac{C}{5}$  Anode**

Similar to the  $\frac{C}{10}$  samples, the  $\frac{C}{5}$  sample shows an appreciable loss of charge capacity, which is more pronounced at the higher C-rate. However, cracks are visible in approximately 15 images taken over 4 different samples. This could be indicative of a diffusion gradient causing a flow or reaction fracture event (Grantab et al, 2011; Brassart et al, 2012). Additionally, the cracks could indicate that particle swelling has occurred in a plastic fashion, permanently reshaping the hard carbon (Milne et al, 2003). These cracks also do not show any natural planes of separation, suggesting that conchoidal fracture has occurred (Atkinson, 1987). This is a characteristic of amorphous materials undergoing fracture events. However, without examining the interior for arrest lines, this is speculation. These cracks, then, cause the fractures to develop along with SEI creation and a loss of capacity. Further testing at C-rates of  $\frac{C}{4}$  and  $\frac{C}{3}$  shows a slight increase in



the number of cracks compared to the  $\frac{C}{5}$  anodes. However, the difference in C-rate is so small that this increase is lost in the noise of the data analysis.

Once a  $\frac{C}{2}$  rate is applied, the reversible capacity decreases even more. Even though the number of cracks in these samples is similar to the previous anode, a  $\frac{C}{2}$  anode has 81% of the first cycle capacity of a  $\frac{C}{5}$  anode. This event could be caused by an inhomogeneous anode mixture, creating regions where ion and electron transport are limited. This creates a local diffusion gradient in that area and subsequent cracks. This hypothesis will be expanded on in **Section IV.E**. **Figures 13** and **14** give the charge capacity data and an image of a sample  $\frac{C}{2}$  anode.

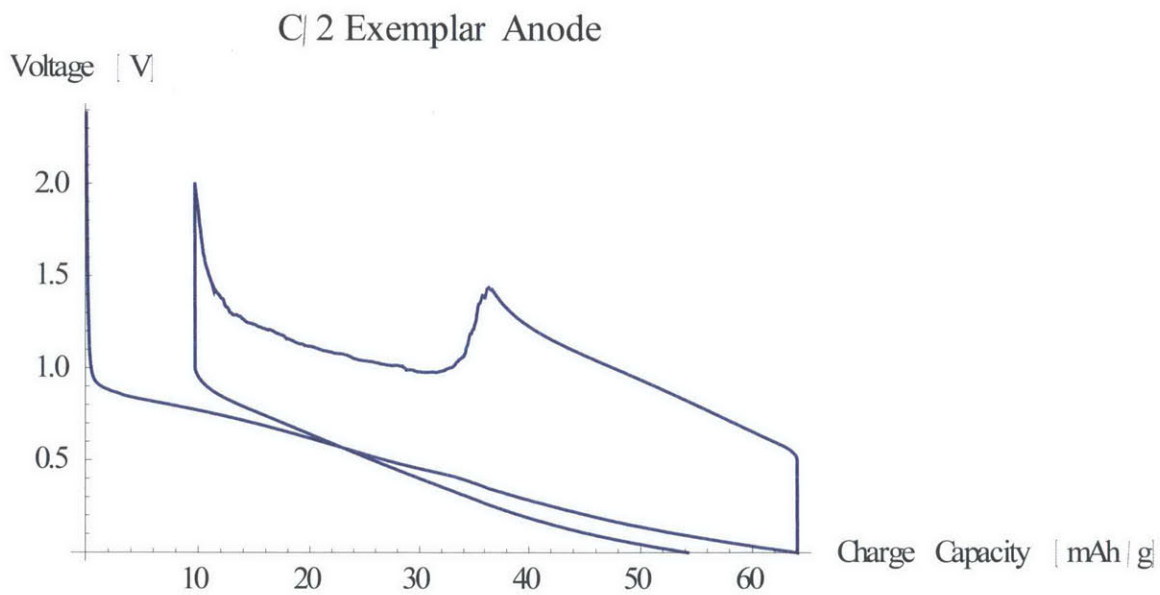


**Figure 13 – Cycling Data for a  $\frac{C}{2}$  Anode**

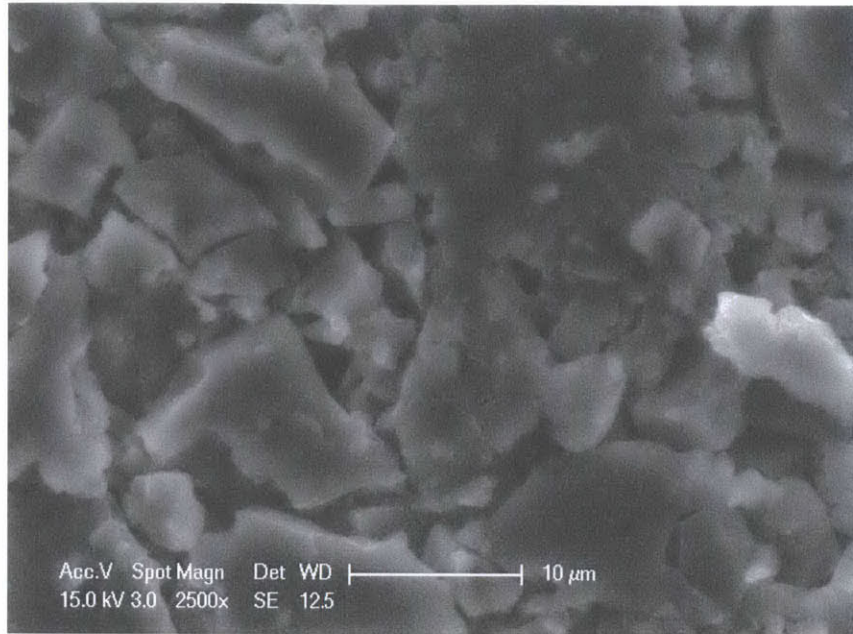


**Figure 14 – SEM Image for a  $\frac{C}{2}$  Anode**

In this particular anode, another phenomenon occurred and is visible at lower magnification as seen in **Figure 15**.

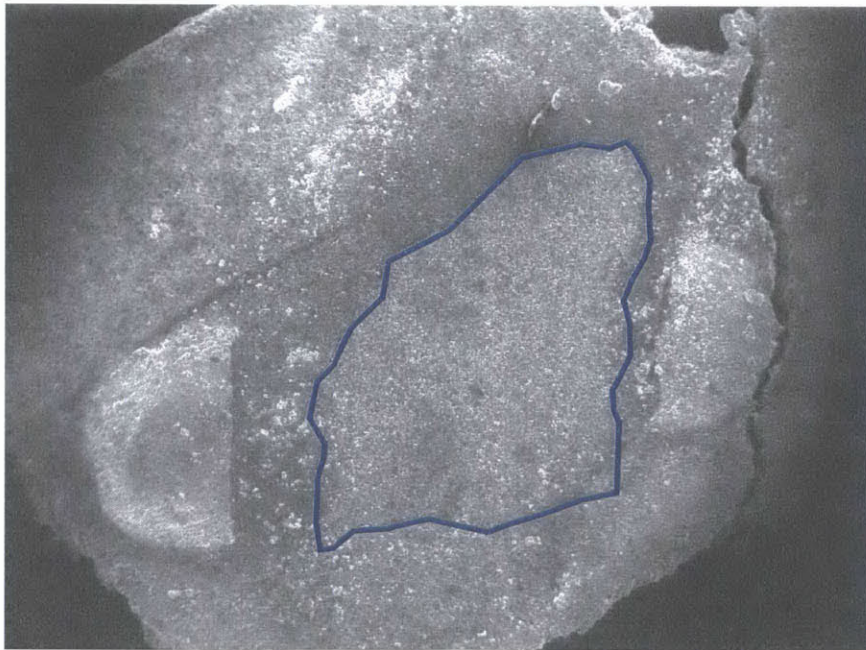


**Figure 15 – Regions of High Intensity Intercalation**

Upon looking at this anode, a high contrast area with jagged morphology is present in the blue outlined area. This outlined area was the section that contained a large majority of fractured particles. This implies that this area was in more contact with the lithium anode than other areas, potentially trapping larger amounts of lithium ions irreversibly. The contrast could be caused by the presence of SEI which does not conduct electricity well and would show up as an insulator in an SEM (Tasaki et al, 2009; Agruba et al, 2013). Due to the uneven contact with the lithium, it cannot then be assumed that the C-rate for this cell was strictly  $\frac{C}{2}$ . There are regions that are perhaps  $\frac{C}{2}$ , but it would be prudent to assume that this specific area should have a C-rate above  $\frac{C}{2}$ . Unfortunately, it is not possible to accurately estimate the C-rate in this area without being able to examine the remainder of the electrode.

Another anode was tested at a C-rate of 5C to examine how a very high C-rate, relative to the stable  $\frac{C}{10}$ , would affect an anode. To start the cycling data for the 5C anode is present in **Figure 16**.

**16.**

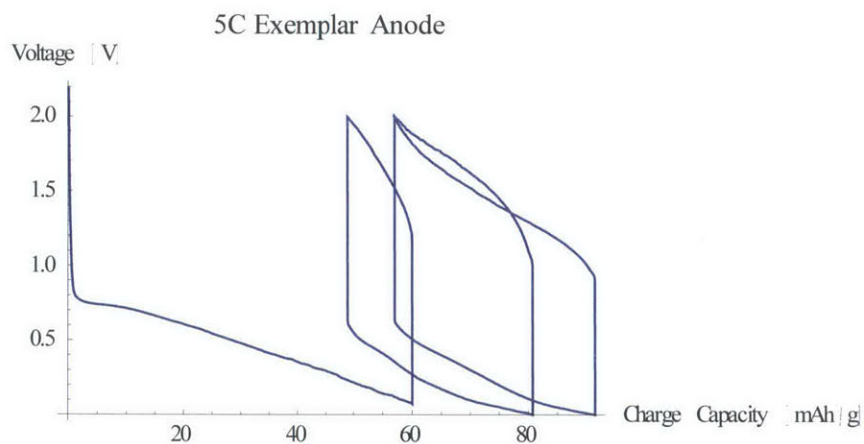


**Figure 16 – 5C Anode Cycling Data**



Following a similar trend to previous anodes, the higher C-rate is causing irreversible capacity loss in the anode. However, it is similar to the capacity seen in a  $\frac{C}{2}$  anode. Looking at the anode in **Figure 17**, though, the anode shows signs of large amounts of fracture and the presence of SEI beginning to blanket certain areas in the image. A reasonable assumption can be made that this SEI also covers more fracture events because fractures act as growth sites for SEI (Agruba et al, 2013).

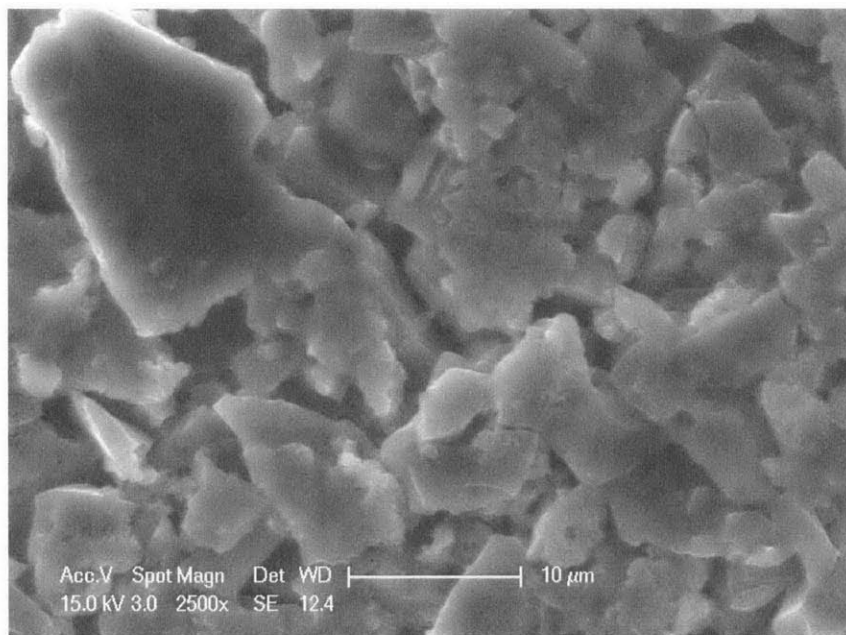


**Figure 17 – 5C Anode SEM Image**

## **Section IV.C – Diffusion Based Current Spikes**

In cycling these hard carbon anodes, a diffusion effect must be taken into account when looking at the current density near the separator and the remainder of the anode (Fuller et al, 1994).

Even though the system is setup to run at  $X \frac{A}{cm^2}$  (where X is some random positive value), that is only the nominal value for the system. Due to kinetic and transport processes, the anode near

the separator experiences a higher current density as a backlog of ions forms at the electrolyte and anode interface. This means the effective current density and C-rate at the interface is higher than the nominal value. In the Fuller et al paper, a model is developed that simulates the motion of ionic flow and consequently the areas where current spikes are present. They note that carbon has the ability to quickly establish a uniform current density; however, the model they created (Figure 7 in their paper) shows a maximum 10% decrease of ionic lithium relative to the rest of the anode when the anode is discharging. Conversely, this implies a local 10% increase in ionic lithium when charging and 10% local current density increase (Fuller et al, 1994). Therefore, the carbon particles adjacent to the separator experience  $1.1X \frac{A}{cm^2}$  and a 1.1X C-rate, compared to the nominal value of the system.

A possible special case involving this phenomena was seen in the crack in the  $\frac{C}{10}$  anode. If it is assumed that the anode does not have a uniform surface, then only a portion of the anode is initially intercalating lithium ions. This effect can then be compounded with the limited surface area current spike to produce a crack a C/10 anode. Another case of this was seen in **Figure 15** where regions of SEI are present on the surface of the anode. The compounding effects of a surface current spike and a limited surface area current spike allow SEI to form on this region due to the high current input at the surface of the anode (Agruba et al, 2013).

## **Section IV.D – Fracture Count Data Analysis**

Based on the analysis of 25 different images at 2500X, a total number of particles was acquired. In order for a particle to be valid, it must have been at least 3 micrometers in size or larger. This

number was used to determine an average number of particles per image by dividing the total number of particles counted by the number of images sampled. Consequently, the average number of particles per image is  $24 \pm 3$  particles. Afterwards, each image was sampled for cracks. Any crack that appears to either completely or partially split a hard carbon particle would be considered a fracture event. Additionally, if two cracks meet on a particle of carbon and the cracks appear to have different points of origin (i.e. – different notches or pits), there will only be one fracture event counted as the cracks have broken one particle. An example of fractures can be seen in **Figure 18** with all of the cracks highlighted in red.

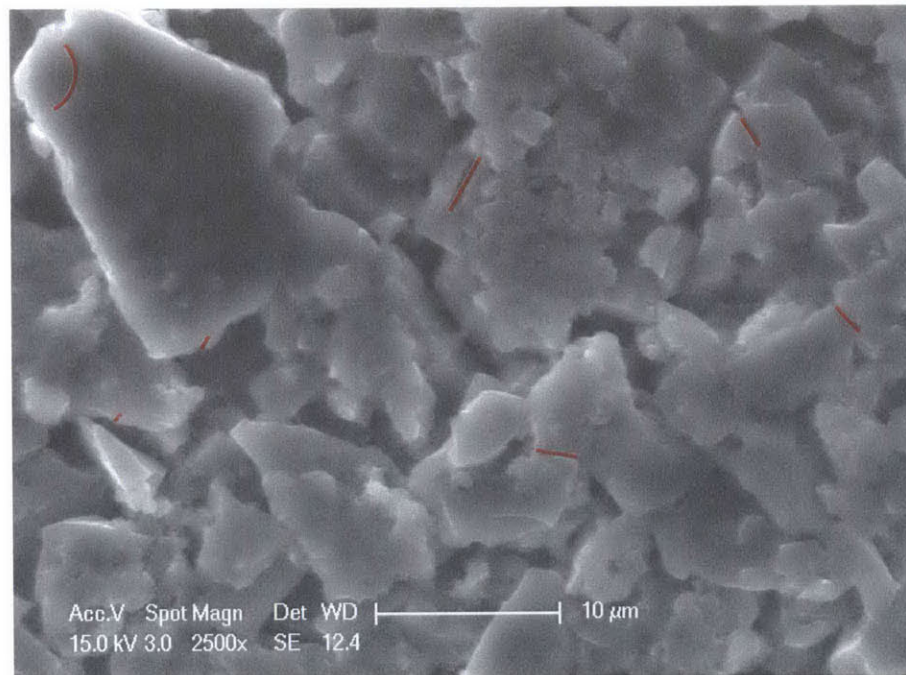


**Figure 18 – Exemplar Image with Highlighted Cracks**

The summary of fracture events in relation to sample size and C-rate can be seen in **Table 2**. In the table, the total sum of particles is calculated for each C-rate by multiplying the number of images times the approximate number of particles per image. Subsequently, the total number

of cracks is summed. This is done to simulate a large anode surface with a total number of particles and cracks. Then, the percentage of cracked particles is calculated. This is done by dividing the number of cracked particles by the number of total particles. Error is calculated by taking the standard deviation of a binary measure where the total number of particles, N, is the population size and the total number of fractures is the number of successful events, M. The formula for this is in **Equation 3**:

$$\text{Percent Error} = \frac{\sqrt{\left(\frac{M}{N}\right) * \left(1 - \left(\frac{M}{N}\right)\right)}}{N} * 100$$

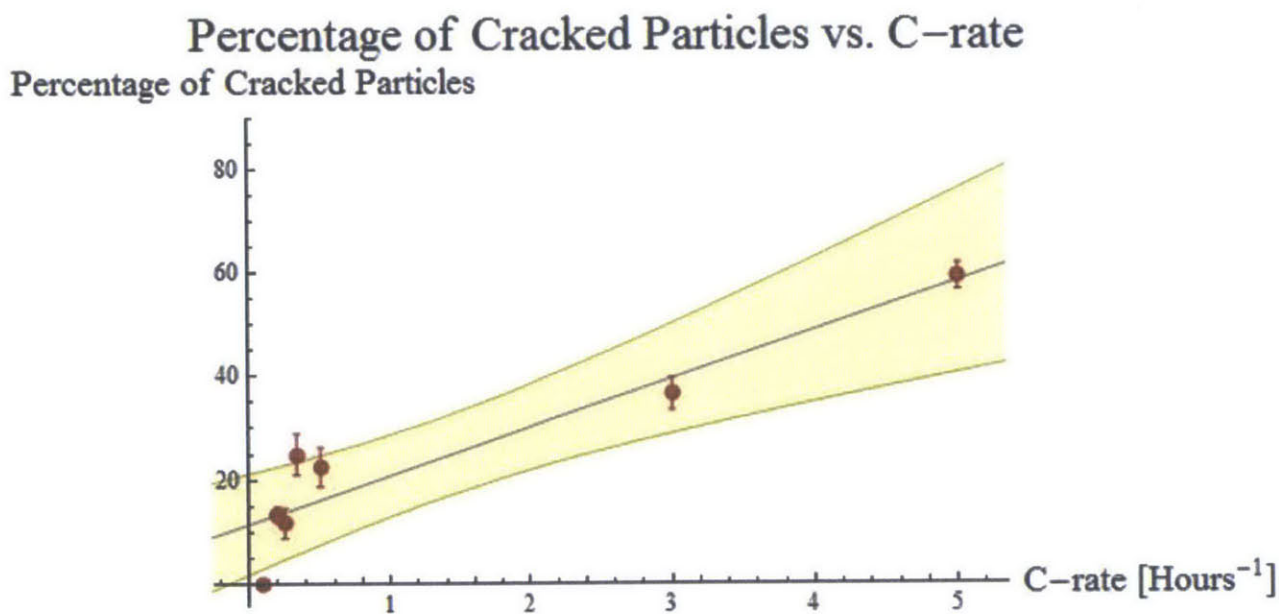
**Equation 3 – Standard Error for Binary Value System**

This can be done because either a particle is fractured, thus having a zero value, or it is not fractured, a one value, allowing it to become a Bernoulli variable.

C-rate Applied to Cell	Local C-rate	Number of Images Analyzed	Total Number of Particles	Total Number of Cracks Present	Average Percentage of Particles Fractured
$\frac{C}{10}$	0.11C	20	480	1	0 ± 0.2%
$\frac{C}{5}$	0.22C	20	480	64	13.3 ± 1.5%
$\frac{C}{4}$	0.275C	5	120	14	11.7 ± 2.9%
$\frac{C}{3}$	0.366C	5	120	30	25.0 ± 4.0%
$\frac{C}{2}$	0.55C	5	120	27	22.5 ± 3.8%
3C	3.3C	10	240	88	36.6 ± 3.1%
5C	5.5C	15	360	213	59.2 ± 2.6%

**Table 2 – Summary of Data Collected**

The percentages of fractured particles were put onto a plot, aligned to their respective C-rates and were fitted to a curve. **Figure 19** is the plot that tries to establish a relationship between the nominal C-rate of anodes and the percentage of fractured particles at a specified C-rate. Additionally, **Figure 20** gives numerical data concerning the plot in **Figure 19**. Each red point in the plot shows a percentage of cracked particles at a specific C-rate along with its statistical error. The blue line represents a linear fit that can describe the increase in crack percentage as a function of C-rate. The filled-in yellow area is a 95% confidence envelope which attempts to map out a zone where possible data points could appear.



**Figures 19 – Plot of Average Number of Cracks as a Function of C-rate**

Best Linear Fit:	$11.47 + 9.379 X$	Equation that minimizes sum of square differences between data points and line
R-squared:	0.8588	Measure of correlation of the y-values with x: $1 - R\text{-squared} = (\text{fitting variance})/(\text{data variance})$
Intercept error:	3.774	Standard deviation for b in $y = mX + b$
Slope error:	1.701	Standard deviation for m in $y = mX + b$
Model P-value	0.002683	Probability that the data are *not* correlated.

**Figure 20 – Plot Analysis of Figure 19**

**Figure 19** shows a correlation between an increase in C-rate and the number of cracks that result. This is demonstrated by the R-squared value and the presence of most points within the 95% confidence envelope. More specifically, it estimates that for every 1C increase, 9 percent more of the particles in the system will fracture. Based on the data, below a  $\frac{C}{10}$  rate no fractures occur. Oddly, though, the linear fit estimates that 10% of the particles are already pre-cracked prior to the application of current. This implies that cracks already preexist on the surface of the hard carbon prior to cycling, possibly as microcracks that cannot be detected via SEM imaging (Kawamura et al, 1972). This could be caused by the process used to make the hard carbon, which gives the structure an inherent jagged morphology (Xing et al, 1996). Additional anode sampling and imaging could help to verify this idea. Another item to note is the rapid increase of fracturing in low C-rate anodes (0.2, 0.25, and 0.33 C) which then tapers off. This section of the data is the most varied when compared to the overall linear trend and has the only point that it above the 95% confidence envelope. Possible answers to this event include the following two options. Firstly, a possible inhomogeneity within a sample anode can cause the local C-rate to spike more than normal (Renganathan et al, 2010). This is due to an abnormal distribution of electron and ion transport rates among local particles. In turn, the inhomogeneity creates a large amount of cracking to occur due to the large diffusion gradient that develops (Zhao et al, 2010). Due to the small sample size, this then skews the data from a more accurate value. A second possibility is the hard carbon's irregular shape and processing techniques creating a large variation of flaw sizes that can be exploited by electrochemical shock. Kawamura and associates discuss in their paper the flaws in glassy carbon fibers that develop during the pyrolysis of phenolic resins. In Kureha's materials, they note that petroleum pitch is used to



make the hard carbon. Assuming similar reactions happen in both the resin and pitch pyrolyses, it can be assumed that cracks could develop in the pyrolytic process. Once water and other gaseous molecules are burned out of the hydrocarbons, a volume shrinkage will most likely occur as the systems coalesce. Coupling the shrinkage with further mechanical processing (i.e. – milling, spinning, etc.) or volatile outgassing allows flaws to develop on the surfaces of the materials that may not be noticeable until further stressing propagates their status (Kawamura et al, 1972). Kawamura concludes by saying that cracks as small as  $4.0 \times 10^{-6}$  cm could be the main source of cracking in glassy carbon fibers. Assuming that the hard carbon used has similar properties to the glassy carbon fibers, it could be that the critical flaw size could be on the order of  $10^{-5}$  or  $10^{-6}$  cm, something not easily detectable in an SEM.

## Section IV.E – Results Comparison to Theoretical Model

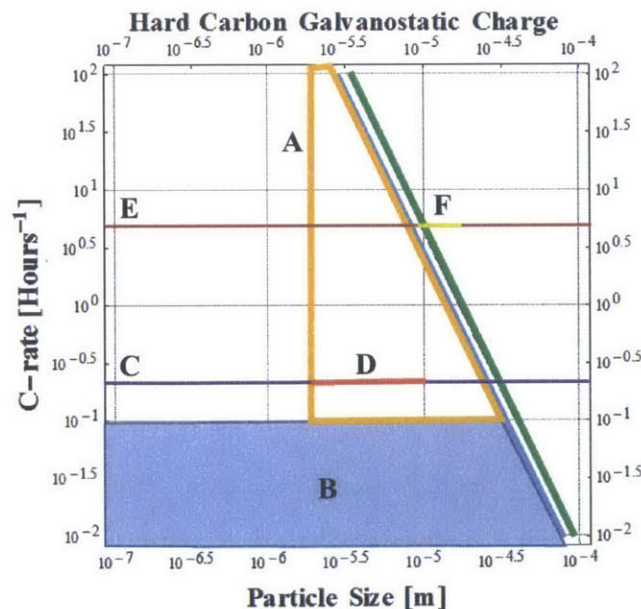


Figure 21 – Hard Carbon Electrochemical Shock Map Check

In comparing the SEM images to the fracture model, it appears that the model, **Figure 21**, is correct to some extent. The orange polygon, **A**, outlines the conditions where theoretically no fracture should occur in the anodes. The limits for this are the lower bound particle size (three micrometers) established when counting hard carbon particles (the leftmost orange line in the polygon) and the experimentally observed fracture lower bound (the top line of the shaded blue area), **B**. However, in analyzing the  $\frac{C}{5}$  images, cracks exist in particles that are smaller than ten micrometers. The  $\frac{C}{5}$  condition is shown in **Figure 21** as the purple line, **C**, and observed particles that fractured are the red line, **D**. In these events, the particles which fractured tended to be larger (above ten micrometers); however, some smaller particles did crack (below 5 micrometers). The inhomogeneous explanation used in **Section IV.E** can be used to account for these events. Similarly, the 5C images also showed cracked particles that were smaller than ten micrometers. The 5C condition is located at the dark red line, **E**, in **Figure 21**. However, in these images, that was the exception rather than the norm. Most particles that fractured were above the ten micrometer size condition, shown as the yellow line, **F**, in **Figure 21**. This implies that at higher C-rates this current version of the model can better predict the conditions necessary for fracture. Here, perhaps, the larger particles acted as sinks that could remove some of the electrochemical load encountered by the smaller particles (Zhao et al, 2010). One possible explanation for the lack of accuracy throughout the model, though, could be that the geometry assumption made initially is incorrect. It is possible that the irregular shape of the hard carbon prevents any simple geometric assumption, rendering the model prone to error. To fine tune this model for more accurate predictions, then, the input parameters must be adjusted to



account for the unique geometries and material properties of the hard carbon (i.e. – its distinct, jagged shape, amorphous nature, etc.) instead of estimates from other materials.

## Section V

### Conclusion

Hard carbon is an interesting material with potential to act as an anode material that has a very high charge capacity and theoretically is not as susceptible to cyclical failure mechanisms. Its unique microstructure allows it to adsorb lithium ions and has large interlayer spacing, allowing lithium to easily move in and out of its structure. However, under the right conditions, it is still susceptible to brittle fracture. One particularly harmful variable to this anode is a high C-rate. By forcing large amounts of ions onto the surface of the hard carbon, a diffusion induced stress will develop which can cause a crack to form. More importantly, the percentage of cracked particles has been shown to correlate at the rate 9 percent of particles per sample increase every additional 1C. The possible existence of microcracks inherent, seen in **Figure 19**, in these particles also act as a potential source for larger cracks to develop on. Additionally, all anodes must be mixed thoroughly during formulation, otherwise the potential for inhomogeneous sites to develop cracks becomes a problem. Lastly, in conjunction with a more accurate electrochemical shock map, these electrodes can be developed to function within optimal parameters of C-rate and particle size, allowing them to become a feasible material to use in a commercial environment.

## Section VI

### Citations

1. Warne, D.F. (2005). *Newnes Electrical Power Engineer's Handbook* (2nd Edition). (pp. 355,356). Elsevier. Online version available at:  
<http://app.knovel.com/hotlink/toc/id:kpNEPEHE03/newnes-electrical-power>
2. Marom, Rotem, S. Francis Amalraj, Nicole Leifer, David Jacob, and Doron Aurbach. "A Review of Advanced and Practical Lithium Battery Materials." *Journal of Materials Chemistry* 21.27 (2011): 9938. Print.
3. Tasaki, Ken, Alex Goldberg, Jian-Jie Lian, Merry Walker, Adam Timmons, and Stephen J. Harris. "Solubility of Lithium Salts Formed on the Lithium-Ion Battery Negative Electrode Surface in Organic Solvents." *Journal of The Electrochemical Society* 156.12 (2009): A1019. Print.
4. Kureha Battery Materials Japan Company, Limited, "Introduction of KBMJ and Carbotron", Technical Presentation, September 4th, 2013
5. Agubra, Victor, and Jeffrey Fergus. "Lithium Ion Battery Anode Aging Mechanisms." *Materials* 6.4 (2013): 1310-325. Print.
6. Grantab, Rassin, and Vivek B. Shenoy. "Location- and Orientation-Dependent Progressive Crack Propagation in Cylindrical Graphite Electrode Particles." *Journal of The Electrochemical Society* 158.8 (2011): A948. Print.
7. Woodford, William H., Yet-Ming Chiang, and W. Craig Carter. "'Electrochemical Shock' of Intercalation Electrodes: A Fracture Mechanics Analysis." *Journal of The Electrochemical Society* 157.10 (2010): A1052. Print.
8. Bottani, Eduardo J. Tascón, Juan M.D. (2008). *Adsorption by Carbons - Novel Carbon Adsorbents*. (pp. 595,596). Elsevier. Online version available at:  
<http://app.knovel.com/hotlink/toc/id:kpACNCA005/adsorption-by-carbons>
9. Brassart, Laurence, and Zhigang Suo. "Reactive Flow In Large-Deformation Electrodes Of Lithium-Ion Batteries." *International Journal of Applied Mechanics* 04.03 (2012): 1250023. Print.
10. Zhang, Xiangc Ann Marie Sastry, and Wei Shyy. "Intercalation-Induced Stress and Heat Generation within Single Lithium-Ion Battery Cathode Particles." *Journal of The Electrochemical Society* 155.7 (2008): A542. Print.
11. Hu, Yuhang, Xuanhe Zhao, and Zhigang Suo. "Averting Cracks Caused by Insertion Reaction in Lithium-ion Batteries." *Journal of Materials Research* 25.06 (2010): 1007-010. Print.

12. Zhao, Kejie, Matt Pharr, Joost J. Vlassak, and Zhigang Suo. "Fracture of Electrodes in Lithium-ion Batteries Caused by Fast Charging." *Journal of Applied Physics* 108.7 (2010): 073517. Print.
13. Klink, Stefan. "In-depth Analysis of Irreversible Processes in Lithium Ion Batteries." Diss. Ruhr-Universität Bochum, 2013. Print.
14. Boris Markovsky, Mikhail D. Levi, Doron Aurbach, The basic electroanalytical behavior of practical graphite–lithium intercalation electrodes, *Electrochimica Acta*, Volume 43, Issues 16–17, 29 May 1998, Pages 2287-2304, ISSN 0013-4686, [http://dx.doi.org/10.1016/S0013-4686\(97\)10172-4](http://dx.doi.org/10.1016/S0013-4686(97)10172-4).
15. L Rapoport, I Lapsker, L Levin, Crack propagation in nitrogen-implanted glassy carbon observed during scratch testing, *Surface and Coatings Technology*, Volume 105, Issues 1–2, 5 June 1998, Pages 117-124, ISSN 0257-8972, [http://dx.doi.org/10.1016/S0257-8972\(98\)00467-8](http://dx.doi.org/10.1016/S0257-8972(98)00467-8).
16. Sglavo, V. M., and D. J. Green. "ChemInform Abstract: Threshold Stress Intensity Factor (K<sub>th</sub>) in Soda-Lime Silicate Glass by Interrupted Static Fatigue Test." *ChemInform* 27.47 (1996): No. Print.
17. Nadeau, J. S. "Subcritical Crack Growth in Vitreous Carbon at Room Temperature." *Journal of the American Ceramic Society* 57.7 (1974): 303-06. Print.
18. Pharr, George M., Daniel L. Callahan, Shaun D. Mcadams, Ting Y. Tsui, Simone Anders, André Anders, Joel W. Ager, Ian G. Brown, C. Singh Bhatia, S. R. P. Silva, and John Robertson. "Hardness, Elastic Modulus, and Structure of Very Hard Carbon Films Produced by Cathodic-arc Deposition with Substrate Pulse Biasing." *Applied Physics Letters* 68.6 (1996): 779. Print.
19. Guo, Hua-Jun, Xin-Hai Li, Xin-Ming Zhang, Hong-Qiang Wang, Zhi-Xing Wang, and Wen-Jie Peng. "Diffusion Coefficient of Lithium in Artificial Graphite, Mesocarbon Microbeads, and Disordered Carbon." *New Carbon Materials* 22.1 (2007): 7-10. Print.
20. Stevens, D. A., and J. R. Dahn. "High Capacity Anode Materials for Rechargeable Sodium-Ion Batteries." *Journal of The Electrochemical Society* 147.4 (2000): 1271. Print.
21. Stevens, D. A., and J. R. Dahn. "The Mechanisms of Lithium and Sodium Insertion in Carbon Materials." *Journal of The Electrochemical Society* 148.8 (2001): A803. Print.
22. Azuma, Hideto, Hiroshi Imoto, Shin'ichiro Yamada, and Koji Sekai. "Advanced Carbon Anode Materials for Lithium Ion Cells." *Journal of Power Sources* 81-82 (1999): 1-7. Print.
23. Yoshio Nishi, Lithium ion secondary batteries; past 10 years and the future, *Journal of Power Sources*, Volume 100, Issues 1–2, 30 November 2001, Pages 101-106, ISSN 0378-7753, [http://dx.doi.org/10.1016/S0378-7753\(01\)00887-4](http://dx.doi.org/10.1016/S0378-7753(01)00887-4).

24. Nalimova, V., D. Guérard, M. Lelaurain, and O. Fateev. "X-ray Investigation of Highly Saturated Li-graphite Intercalation Compound." *Carbon* 33.2 (1995): 177-81. Print.
25. Milne, I. Ritchie, R.O. Karihaloo, B. (2003). *Comprehensive Structural Integrity, Volumes 1-10.* (pp. 509). Elsevier. Online version available at:  
<http://app.knovel.com/hotlink/toc/id:kpCSIV0002/comprehensive-structural>
26. Atkinson, Barry Kean (1987). *Fracture Mechanics of Rock.* (pp. 39). Elsevier. Online version available at: <http://app.knovel.com/hotlink/toc/id:kpFMR00001/fracture-mechanics-rock>
27. Fuller, Thomas F., Marc Doyle, and John Newman. "Simulation and Optimization of the Dual Lithium Ion Insertion Cell." *Journal of The Electrochemical Society* 141.1 (1994): 1. Print.
28. Xing, Weibing, J. S. Xue, Tao Zheng, A. Gibaud, and J. R. Dahn. "Correlation Between Lithium Intercalation Capacity and Microstructure in Hard Carbons." *Journal of The Electrochemical Society* 143.11 (1996): 3482. Print.
29. Kawamura, K., and G. M. Jenkins. "Mechanical Properties of Glassy Carbon Fibres Derived from Phenolic Resin." *Journal of Materials Science* 7.10 (1972): 1099-112. Print.
30. Renganathan, Sindhuja, Godfrey Sikha, Shriram Santhanagopalan, and Ralph E. White. "Theoretical Analysis of Stresses in a Lithium Ion Cell." *Journal of The Electrochemical Society* 157.2 (2010): A155. Print